Supplementary Information: Quantum walks of two correlated photons in a 2D synthetic lattice

Chiara Esposito,[1] Mariana R. Barros,[1,2] Andrés Durán Hernández,[1,3] Gonzalo Carvacho,[1] Francesco Di Colandrea,[2] Raouf Barboza,[2] Filippo Cardano,[2,*] Nicolò Spagnolo,[1] Lorenzo Marrucci,[2] and Fabio Sciarrino[1,4,†]

[1]*Dipartimento di Fisica, Sapienza Università di Roma, Piazzale Aldo Moro 5, I-00185 Roma, Italy*
[2]*Dipartimento di Fisica "Ettore Pancini", Università degli studi di Napoli Federico II,*
Complesso Universitario di Monte S. Angelo, via Cintia, 80126 Napoli, Italy
[3]*Université Paris-Saclay, ENS Paris-Saclay, Département de Physique, 91190 Gif-sur-Yvette, France*
[4]*Consiglio Nazionale delle Ricerche, Istituto dei sistemi Complessi (CNR-ISC), Via dei Taurini 19, 00185 Roma, Italy*

Supplementary Note 1.   Theoretical background

The realization of a quantum walk on a 2D square lattice is performed by the repetitive action of an unitary single-step operator U on a quantum system. Tracing a parallel with the classical random walk, the quantum system plays the role of the walker while its internal spin-like degree of freedom represents the coin [1]. Therefore, the walker can be described by a quantum state $|\psi\rangle$ in the bipartite Hilbert space $\mathcal{H} = \mathcal{H}_p \otimes \mathcal{H}_c$. The two dimensional internal degree of freedom space, $\mathcal{H}_c$, is spanned by the states $\{|\uparrow\rangle, |\downarrow\rangle\}$, and the position space $\mathcal{H}_p$ by $\{|m,n\rangle\}$, where (m,n) label the square lattice coordinates. Thus, the discrete-time quantum walk evolution at the t-th step can be expressed as:

$$|\psi_t\rangle = U^t |\psi\rangle. \tag{1}$$

The single-step operator U encompasses the spin rotation $C(\omega)$, which only acts on the coin space, and the spin-dependent translation operators along x and y directions, T_d, with $d = x, y$. The general unbalanced spin rotation is given by :

$$C(\omega) = \mathbb{I}_p \otimes \begin{pmatrix} \cos(\omega) & \imath \sin(\omega) \\ \imath \sin(\omega) & \cos(\omega) \end{pmatrix}, \tag{2}$$

where parameter ω sets the balance of the coin rotation. In a balanced coin rotation, there is an equal probability to move in each direction, condition achieved if $\omega = \pi/4$.
The translation operator can be expressed as:

$$T_d(\delta) = \cos\frac{\delta}{2}\mathbb{I} + \imath \sin\frac{\delta}{2}S_d, \tag{3}$$

where δ establishes the probability of the walker to remain in the same position at each step, while the operator S_d is the shift operator along the $d = x, y$ direction. The S_x operator does not act on y coordinates and it is given by:

$$S_x = \sum_{m,n} |m-1,n,\uparrow\rangle \langle m,n,\downarrow| + |m+1,n,\downarrow\rangle \langle m,n,\uparrow|. \tag{4}$$

Similarly, the operator S_y does not act on x coordinates and is defined as $S_y = \sum_{m,n} |m,n-1,\uparrow\rangle \langle m,n,\downarrow| + |m,n+1,\downarrow\rangle \langle m,n,\uparrow|$. The ordering of these operators in the single-step operator U and the chosen values for δ and ω allows to define different QWs protocols.
Here, we mainly focused on the 2D-QW protocol $U = T_y(\delta)C(\omega)T_x(\delta)C(\omega)$, setting $\delta = \pi$ and $\omega = \pi/4$. By making this choice, we selected a protocol in which the walker must change its position at each step, with a balanced coin rotation.
In the particular case of one-particle regime, we considered a family of localized initial states $|\psi_0\rangle$ described by:

$$|\psi_0\rangle = \cos\frac{\alpha}{2} |1,0,\uparrow\rangle + \imath \sin\frac{\alpha}{2} |1,0,\downarrow\rangle. \tag{5}$$

From the evolved state, $|\psi_t\rangle$, we obtained the probability distribution as:

$$P^{(t)}(\mathbf{r}) = \sum_{\sigma=\uparrow,\downarrow} |\langle \mathbf{r}, \sigma | \psi_t \rangle|^2, \tag{6}$$

---

[*] filippo.cardano2@unina.it
[†] fabio.sciarrino@uniroma1.it

where the vector $\mathbf{r}$ indicates the positions (m, n) in the lattice.

In the two-particle regime, partial photon indistinguishability has to be taken into account to properly model the input state and calculate theoretical predictions. For two-photon inputs, this effect can be modeled with a density matrix defined as:

$$\rho_0 = c_0 \rho_{\text{ind}} + (1 - c_0) \rho_{\text{dis}}, \tag{7}$$

where ρ_{ind} indicates the density matrix of two completely indistinguishable photons and ρ_{dis} is the density matrix describing two distinguishable particles. The c_0 parameter sets the degree of indistinguishability between the two photons, which is defined in the range $[0, 1]$. At each step, we obtain a probability distribution on the lattice position of the two walkers as:

$$P^{(t)}(\mathbf{r}_1, \mathbf{r}_2) = \sum_{\sigma_1, \sigma_2 = \uparrow, \downarrow} \text{Tr}(\rho_t \,|\mathbf{r}_1, \sigma_1, \mathbf{r}_2, \sigma_2\rangle \,\langle \mathbf{r}_1, \sigma_1, \mathbf{r}_2, \sigma_2|). \tag{8}$$

At each step, the elaboration of the theoretical prediction for the distributions shown in the main text was performed by using Supplementary Equations (6) and (8).

Supplementary Note 2. g-plate Technology

The key elements of our quantum walk are the g-plates [2], which are electrically controlled liquid-crystal waveplates for which the optic axis orientation is varying linearly along one of the in-plane directions. By using the same principle of the *q-plates* [3], an optimally tuned g-plate splits a light beam into two orthogonally polarized beams, as depicted in Fig.2 of the main text. The relative angle between the two split beams is determined by the diffraction-grating spacing of the g-plate, and it is approximately equal to $\alpha = 2\lambda/\Lambda$, where λ is the wavelength of the input beam and Λ the characteristic parameter of the device, defined during the fabrication process. Thus, such device adds a fixed transverse momentum component ($\Delta k_\perp = 2\pi/\Lambda$) to an input beam, and the sign of the "kick" depends on its polarization state. In particular, if the beam is right-handed circularly polarized ($|R\rangle$), it acquires a negative component of the transverse momentum. On the other hand, a left-handed circularly polarized beam ($|L\rangle$) acquires a positive fixed component of the transverse momentum. The action of an x-oriented g-plate in the polarization space is given by the following matrix, written in the circular basis ($|R\rangle, |L\rangle$):

$$G_p = \begin{pmatrix} \cos(\delta/2) & \imath \sin(\delta/2) \, e^{\imath \Delta k_\perp x} \\ \imath \sin(\delta/2) \, e^{-\imath \Delta k_\perp x} & \cos(\delta/2) \end{pmatrix}, \tag{9}$$

where δ is the phase delay introduced by the g-plate, that defines each momentum "kick" probability, and it is tunable by an external programmable voltage source. Finally, the accumulated momentum can be visualized in position space by using a lens system that implements an optical Fourier transformation.

An overall amount of 12 electrically-tuned liquid crystal devices were exploited to perform a two-photon QW up to the third step, encompassing waveplates and g-plates arranged in a cascade configuration. In Supplementary Figure 1 (a) a schematic representation of the exploited apparatus is shown, while the image of a g-plate is reported in Supplementary Figure 1 (b).

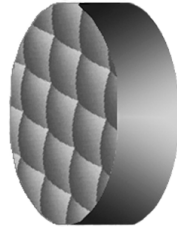### Supplementary Note 3. Micro-lens array

A micro-lens array, model $MLA - S250 - f20$ of RPC Photonics, was used to efficiently inject the photons into the 2D fiber array employed at the detection stage. The micro-lens array is made of polymer-on-glass material, has a size of 250×250 mm^2, index of refraction 1.56 (633 nm), and it is composed of a hundred of micro-lenses with a short effective focal length (around 5 mm), separated by 250 μm (see Supplementary Figure 2). In this way, we were able to reach an individual waist of 15 μm without changing the corresponding distances in the experiment. Consequently, the adoption of such device enabled a significant increase in the coupling efficiency into the final array of optical fibers used for detection from 0.1 to 0.75.

Supplementary Note 4. Experimental implementation

The photons used in the experiment were produced by a parametric source, consisting of a beta-barium-borate (BBO) crystal, that generates a photon pair ($\lambda = 785$ nm) by non-collinear spontaneous parametric down conversion (SPDC) when it is pumped by a pulsed laser with $\lambda = 392.5$ nm. Once the photons were generated by the SPDC source, they were injected into two identical single-mode fibers. Mechanical polarization controllers were employed to arbitrarily and independently control the polarization of each input photon.
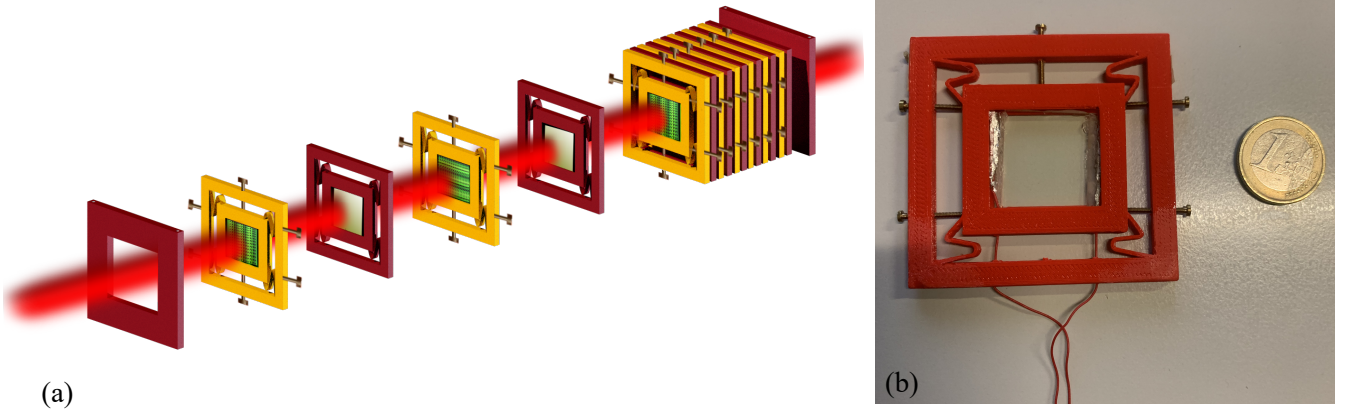
Supplementary Figure 1. **g-plate system.** (a) Schematic view of the quantum walk apparatus used in the experiment. (b) Image of a single g-plate in its mount. The screws on the sides of the red support are exploited to properly align the device orientation with respect to the other g-plates.

Supplementary Figure 2. **Micro-lens array.** Schematic representation of the micro-lens array used to increase the coupling efficiency of the output mode in the fiber array.

In the case of the single-particle 2D-QW, one photon was directly sent thorough a single mode fiber to an Avalanche Photodiode (APD), to be used as trigger. The other photon was sent to the platform at the fiber launch "1", shown in Supplementary Figure 3. It performed the 2D-QW by following the same path as for the 2D-QW with two-photons, presented below. On the other hand, for the case of the two-photon 2D-QW, both particles were injected in the platform. In this case, temporal synchronization of the photons was performed via independent delay lines through an Hong-Ou-Mandel experiment (see Supplementary Note 6). The single-mode fibers were then connected to the fiber launchers "1" and "2", depicted in Supplementary Figure 3. A mirror, mounted on a translation stage, and a half-mirror were used to finely adjust the parallelism between the two beams and to change their relative distance d_0, that can vary from 3 mm to 8 mm. In the sequence, a telescope, composed of two lenses with focal distances $f_1 = 300$ mm and $f_2 = 30$ mm respectively, was used to reduce the beam waist by a factor 10. The relation between the waist and distance can be expressed as following:

$$W_1 = \frac{f_2}{f_1} W_0; \quad d_1 = \frac{f_2}{f_1} d_0. \tag{10}$$

Subsequently, we used a lens with focal distance $f_3 = 2000$ mm to enlarge each waist without changing the separation length. At the output of f_3, each beam had a waist W_2, respecting the following relations:

$$W_2 = \frac{W_1}{\left[1 + (z_1/f_3)^2\right]^{1/2}}; \quad z_1 = \frac{\pi W_1^2}{\lambda}, \tag{11}$$

where z_1 is the Rayleigh length of the beam after the telescope. When $z_1 \ll f_3$, this can be accurately approximated as:

$$W_2 \simeq \frac{\lambda f_3}{\pi W_1} \simeq \frac{\lambda}{\pi W_0} \frac{f_1 f_3}{f_2}. \tag{12}$$
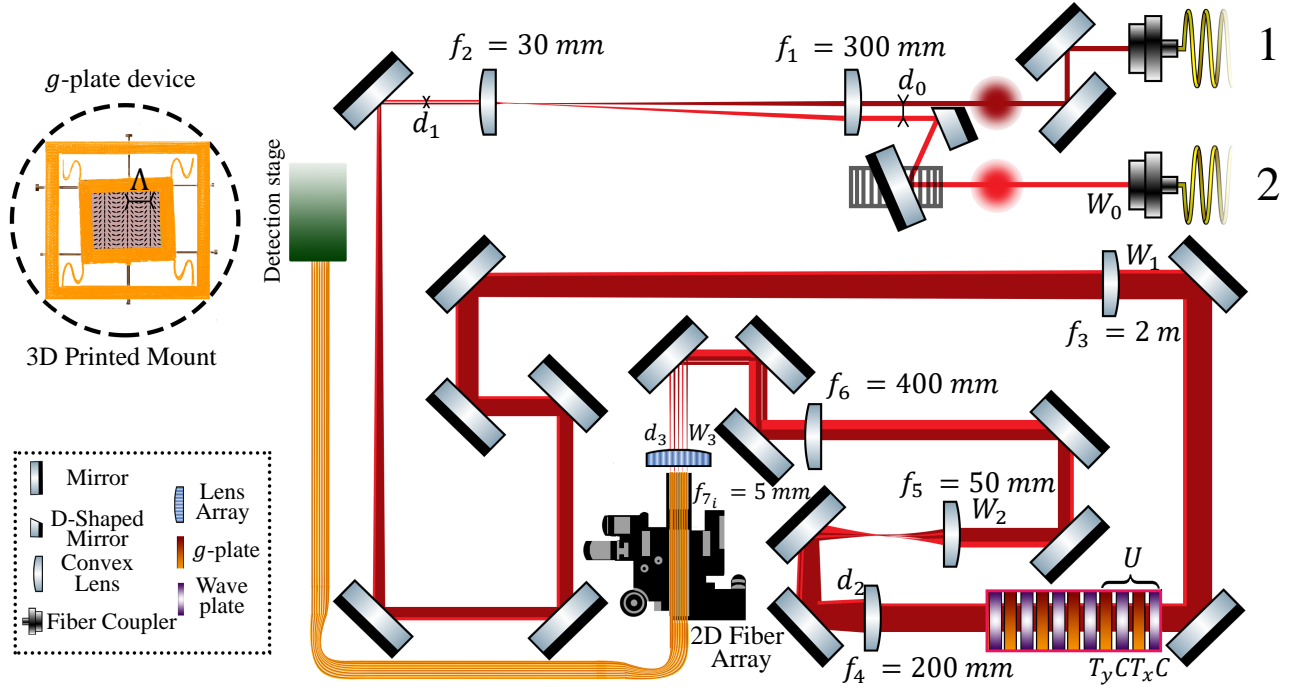
Supplementary Figure 3. **Scheme of the 2 dimensional quantum walk apparatus**. In the single-particle regime, one photon was sent to the fiber coupler "1". For 2D-QW with two walkers, the photons entered the system through ports "1" and "2". A system composed of several mirrors and lenses was properly designed to ensure an efficient coupling into the fiber array, considering the physical constraints imposed by its pitch. After the photons propagate through the g-plates, a micro-lens array was placed immediately before the multimode fiber-array to increase the coupling efficiency.

Therefore, the two beams were highly superposed and collimated. By using the ray transfer-matrix formalism, we were able to compute the relative angle θ_2 between the two beams at the output of f_3, assuming an effective parallelism at the output of f_2:

$$\theta_2 = \frac{d_1}{f_3} = d_0 \frac{f_2}{f_1 f_3}. \tag{13}$$

Hence, by changing the value of d_0, we linearly controlled the input angle between the two beams, θ_2. The angular lattice unity is $\Delta \theta = \lambda/\Lambda$, where Λ is the g-plate characteristic parameter defined above. For $d_0 = 3.14$ cm, the two photons are prepared at $(0,0)$ and $(1,0)$ modes of the quantum walk ($\theta_2 = \lambda/\Lambda = 1.57 \times 10^{-4}$ rad). Thus, increasing by a factor 2 the value of d_0, θ_2 is also magnified by the same factor. In the latter case, the two photons were prepared at $(-1,0)$ and $(1,0)$ input lattice positions. The two-dimensional quantum walk was performed by a cascade of g-plates oriented along the x and y directions, interspersed with waveplates. For n g-plates$_x$ and n g-plates$_y$, the maximum angular difference between two beams is $\theta_{max} = 2 n \Delta \theta$. At the output of the quantum walk structure, we used a three lens system to decrease the relative distance between consecutive beams and reduce their waist. The $f_4 = 200$ mm lens was conjugated with the $f_5 = 50$ mm one to reduce the waist by a factor 4. Then, we used a $f_6 = 400$ mm lens in order to set the subsequent relative distances to d_3 and each waist to W_3.

Given two adjacent beams at the output of the g-plate-system, the angular difference $\Delta \theta$ induces a spatial shift at the focal point of f_6:

$$d_3 = -\Delta\theta \frac{f_4 f_6}{f_5},$$
$$W_3 \simeq \frac{\lambda}{\pi W_2} \frac{f_4 f_6}{f_5}. \tag{14}$$

Numerically, we obtained: $d_3 = 250$ μm and $W_3 = 80$ μm. Hence, the maximum angular shift became a spatial shift equal to $n \times 250$ μm. Finally, we used a micro-lens array (see Supplementary Note 3) to improve the coupling efficiency into the fiber array. We employed a fiber array defining a 8×8 grid, in which the fibers were separated by 250 μm. Each one of these multi-mode fibers has a core of 62.5 μm and its output was coupled to a single-photon avalanche detector.

The measured rate at the output of the SPDC source was approximately 60 kHz single-photon count at each arm, and 6 kHz two-fold events by using a coincidence window of 8 ns. The overall recorded two-fold events after the first, second and third

steps of the quantum walk were 46926, 65611 and 90608. The corresponding coincidence-rates after 1, 2 and 3 steps were 56 Hz, 11 Hz and 7 Hz, respectively. The estimated losses for of the optical apparatus are due to the following optical elements:

- tunable plate (15% for each plate);

- fiber-array coupling (40%);

- delay lines (40% for each photon);

- bunching probabilities detection (around 50%) (See the Supplementary Note 7);

As such, the overall transmission efficiency of the QW evolution (that is considering all liquid crystal devices) is 0.85^N, where N is the number of plates. This yields an efficiency equal to $\simeq 14\%$ after three steps, where $N = 12$. However, by putting a standard anti-reflection coating on plate surfaces, the transmission of a single cell can be increased at least to 95% and the overall efficiency to $\simeq 54\%$.

Supplementary Note 5.   Experimental results for coherent light inputs

For the coherent light data acquisition, we inserted a beamsplitter between the last lens and the micro-lense array, and we positioned the CCD on the reflected path for the image acquisition. We show the raw pictures of one-photon distributions with coherent light in Figure (4b) of the main text. The dark counts of the images are removed by averaging the intensity values of the pixels in a 10×10 pixel square that is far more then 15 lattice steps away from the visible spots. We find the center of each spot of the image by looking for the local maxima of each picture. Then, the waist of each spot is estimated by performing a two-dimensional Gaussian fit on the image data. We calculated the intensity of each light spot in the pictures by summing the intensity value associated to each pixel that belongs to the spot. Then, we divided the latter by the total value of the intensity. In this way, we reconstructed the probability distributions for each step.

Supplementary Note 6.   Photon synchronization through Hong-Ou-Mandel interference

Temporal synchronization between the two-photon paths was performed via a Hong-Ou-Mandel [4] test. Three liquid-crystal plates were exploited as a beamsplitter, following a procedure similar to that reported in Ref. [5] with *q-plates*. In particular, we turned on the plates in the following order: a g-plate along x, a waveplate tuned as $\omega = \pi/4$ and, finally, a g-plate along x. Two identical photons were sent in two adjacent modes $(m+1, 0)$ and $(m-1, 0)$ of the first g-plates with polarization $|R\rangle$ and $|L\rangle$, respectively. We only considered the motion along the x axis and we indicated the state of the photon in the second quantization formalism as $a_{i_x, P}^\dagger |0\rangle$, where i_x is the x coordinate on the lattice and P is the polarization state. The action of the three plates, written in the creation-annihilation operation formalism, reads:

$$
a_{m+1,R}^\dagger \rightarrow \cos\frac{\delta_1}{2}\cos\frac{\delta_2}{2}a_{m+1,V}^\dagger + \frac{\iota}{\sqrt{2}}\cos\frac{\delta_1}{2}\sin\frac{\delta_2}{2}(a_{m+2,R}^\dagger - a_{m,L}^\dagger)+ \\
+\iota\sin\frac{\delta_1}{2}\cos\frac{\delta_2}{2}a_{m,H}^\dagger - \frac{1}{\sqrt{2}}\sin\frac{\delta_1}{2}\sin\frac{\delta_2}{2}(a_{m+1,R}^\dagger + a_{m-1,L}^\dagger),
\tag{15}
$$

and:

$$
a_{m-1,L}^\dagger \rightarrow \cos\frac{\delta_1}{2}\cos\frac{\delta_2}{2}a_{m-1,H}^\dagger + \frac{\iota}{\sqrt{2}}\cos\frac{\delta_1}{2}\sin\frac{\delta_2}{2}(a_{m,R}^\dagger + a_{m-2,L}^\dagger)+ \\
+\iota\sin\frac{\delta_1}{2}\cos\frac{\delta_2}{2}a_{m,V}^\dagger - \frac{1}{\sqrt{2}}\sin\frac{\delta_1}{2}\sin\frac{\delta_2}{2}(a_{m+1,R}^\dagger - a_{m-1,L}^\dagger).
\tag{16}
$$

Hence, the two-photon probability of having a bunching event in the initial positions $x_1 = m+1$ and $x_2 = m-1$ becomes:

$$
P_b(m+1, m-1) = P(m+1, m+1) + P(m-1, m-1) = \left(\cos\frac{\delta_1}{2}\cos\frac{\delta_2}{2}\sin\frac{\delta_1}{2}\sin\frac{\delta_2}{2}\right)^2 + \left(\sin\frac{\delta_1}{2}\sin\frac{\delta_2}{2}\right)^2.
\tag{17}
$$

In Supplementary Figure 4 (a) we show the plots of the bunching probability as a function of the tuning parameters δ_1 and δ_2. For $\delta_1 = \delta_2 = \pi$ the probability of bunching is equal to 1. For this value of the g-plates tuning, the plates mimic a beamsplitter with transitivity $t = 1/\sqrt{2}$, in the subspace of g-plate modes $(m+1, R), (m-1, L)$:

$$
M_G = \begin{pmatrix} 1/\sqrt{2} & 1/\sqrt{2} \\ 1/\sqrt{2} & -1/\sqrt{2} \end{pmatrix},
\tag{18}
$$
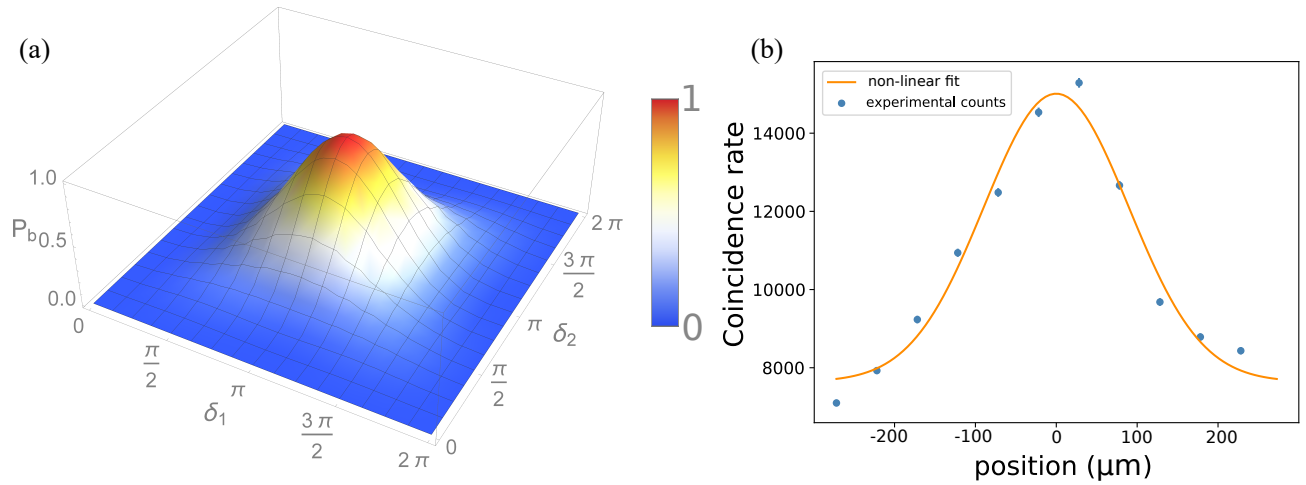
Supplementary Figure 4. **Hong-Ou-Mandel test for photon path synchronization**. (a) We plot the probability of bunching (P_b) in position $(-1, 0)$ and $(1, 0)$ as a function of the electrical tuning δ_1 and δ_2 of the g-plates. We observe that the bunching probability approaches 1 when $\delta_1 = \delta_2 = \pi$. (b) Experimental verification of photon indistinguishability through Hong-Ou-Mandel (HOM) interference after the quantum walk platform. The poissonian statistical uncertainties are included in the experimental points. The measured visibility of the pattern is $v = 0.95 \pm 0.02$.

that is the matrix representation of a 50/50 beamsplitter.

We experimentally performed the Hong-Ou-Mandel experiment in this configuration. The two photon input state was prepared in lattice sites $(-1, 0)$ and $(1, 0)$ with $|L\rangle$ and $|R\rangle$ polarization, respectively. In particular, we considered one of the two possible outputs of this unitary evolution to measure the bunching configuration. Indeed, for any arbitrary unitary operation, the probability of bunching of two indistinguishable photons exiting from the same output is twice the one obtained with distinguishable ones. More specifically, by considering a generic unitary U and two photons entering in input modes n an m, the probability that the two particles exit from the same output k in the distinguishable and indistinguishable cases are respectively:

$$P_{\text{dis}}(k, k) = |U_{n,k}|^2 |U_{m,k}|^2 \tag{19}$$

$$P_{\text{ind}}(k, k) = 2|U_{n,k}|^2 |U_{m,k}|^2, \tag{20}$$

independently of the unitary matrix. For this reason, the visibility of the HOM peak is independent of the g-plate unitary transformation and only depends on photon indistinguishability. To discriminate the events when two photons exit from the same output we used a 50/50 fiber beamsplitter (FBS). Then, we connected the FBS output ports to two avalanche photo-diodes (APDs). We then acquired the coincidence-rate at different positions of the translation stage. The measured interference pattern is shown in Supplementary Figure 4 (b). The visibility v of the peak was estimated by using the following formula:

$$v = \frac{cc_{\text{in}} - cc_{\text{out}}}{cc_{\text{out}}}, \tag{21}$$

where the cc_{in} and cc_{out} are the coincidence-rates at the maximum and large time separation, respectively. The obtained value of the visibility is 0.95 ± 0.02, showing that the degree of indistinguishability of the photons is not significantly affected by the cascade of g-plates corresponding to the quantum walk platform.

Supplementary Note 7. Experimental results for one- and two- photon inputs

Three steps of the U 2D-QW protocol were performed with one and two photons. The one-particle probability distributions are measured by counting the two-fold events between the photon that performs the quantum walk and the trigger photon. Conversely, the two-photon distributions are obtained from the two-fold events between each pair of output modes. We considered only the modes whose coincidence number is much higher than accindental ones (2 modes for the first step, 6 for the second step and 12 for the third step), as analogously performed in previous experiments [6–8]. In order to measure also the bunching probability we use a fiber beamsplitter for each measured mode. Hence we use two avalanche photodiode detectors for each mode. The fiber beamsplitter allows one to detect bunching configurations, i.e. two photon per mode, with a probability $p = 2t(1 - t)$, where t is the fiber beamsplitter transmissivity. We calculate the error on each distribution value by using a

bootstrapping approach. Then each probability distribution P is obtained by dividing the two-fold events of each pair of modes by the total number of measured events. We remove the accidental coincidences (due to the dark counts) by considering the dark signal as a continuous stochastic signal. The accidental coincidences for each pair of modes $A_{i,j}$ are given by [9]:

$$A_{i,j} = 2S_i S_j T w$$

where S_i and S_j are the values of single-event rates of the i and j modes, T is the total time of the data acquisition and w is the coincidence windows, i.e. the time interval in which we consider two events as simultaneous. Finally, we correct each value with the coupling efficiencies. These corrections are obtained by injecting coherent laser light into each output mode and by calculating the coupling efficiency as the ratio between the output and the input light intensity.

Here, we report the details on the similarity calculation for one- and two-particle regimes. Moreover, we report also the distributions for distinguishable particles. Finally, we show the plots of the non-classicality test, presented in Supplementary Equation (24), in the indistinguishable regime for all the steps. The errors on distributions values and all the derived quantities were calculated via bootstrapping approach, by considering that the distributions values are sampled on a Poissonian probability distribution.

A. One-particle regime

In the one-particle regime, the experiment was carried out by directly detecting one of the two-photons, acting as a trigger, while the other is injected in the quantum-walk platform. The probability distributions were measured at the end of each step, and the steps were performed by inserting the photon with polarization $|D\rangle$ in $(1,0)$. The distributions are shown in the main text. We compared the theoretical and experimental distributions using the similarity defined as:

$$\mathcal{S}_{1p}^{(t)} = \left(\sum_{\mathbf{r}} \sqrt{P^{(t)}(\mathbf{r}) \tilde{P}^{(t)}(\mathbf{r})} \right)^2 , \tag{22}$$

where t is the step number, $\mathbf{r}$ is the particle position on the lattice and $P^{(t)}(\mathbf{r})$ and $\tilde{P}^{(t)}(\mathbf{r})$ are the theoretical and the experimental distributions, respectively.

B. Two-particle regime

In the two-particle regime, the photon paths were synchronized in the g-plate by performing a Hong-Ou-Mandel test (see Supplementary Figure 4). As explained in Supplementary Note 6, such test was performed by exploiting the g-plates as a beamsplitter. The value of the measured visibility was employed to set the value of $c_0 = 0.95$ in the distribution theoretical calculations. Similarly to the one-particle regime, the probability distributions were measured at the end of each step. The steps were performed by injecting the two photons with polarization $|A\rangle$ and $|D\rangle$ in $(-1, 0)$ and $(1, 0)$, respectively. The two-dimensional lattice was linearized to perform a representation of the four-dimensional probabilities, thus presenting the latter quantities as two-parameter functions. The linearization of each lattice site was obtained as the following map $\mathbf{r} \rightarrow m + 7n$ with $m, n \in [-3, 3]$. To report the experimental coincidence-rate matrix, the same linearization was performed. In the main text, we show distributions after each of the three steps for indistinguishable particles, with the corresponding value of similarity. The similarity was calculated by generalizing that corresponding to one particle in the following way:

$$\mathcal{S}_{2p}^{(t)} = \left(\sum_{\mathbf{r}_1, \mathbf{r}_2} \sqrt{P^{(t)}(\mathbf{r}_1, \mathbf{r}_2) \tilde{P}^{(t)}(\mathbf{r}_1, \mathbf{r}_2)} \right)^2 , \tag{23}$$

where t is the step number, $\mathbf{r}_1$ and $\mathbf{r}_2$ are the positions on the lattice of the particle 1 and 2 and $P^{(t)}(\mathbf{r}_1, \mathbf{r}_2)$ and $\tilde{P}^{(t)}(\mathbf{r}_1, \mathbf{r}_2)$ are the theoretical and the experimental distributions, respectively.

In Supplementary Figure 5, the theoretical and experimental distributions for distinguishable particle ($c_0 = 0$) for 1, 2 and 3 steps are shown. The calculated similarities are $\mathcal{S}_{dis}^{(1)} = 0.9997 \pm 0.0001$, $\mathcal{S}_{dis}^{(2)} = 0.9886 \pm 0.0006$ and $\mathcal{S}_{dis}^{(3)} = 0.954 \pm 0.002$, thus proving a good agreement between the expected results and experimental ones.
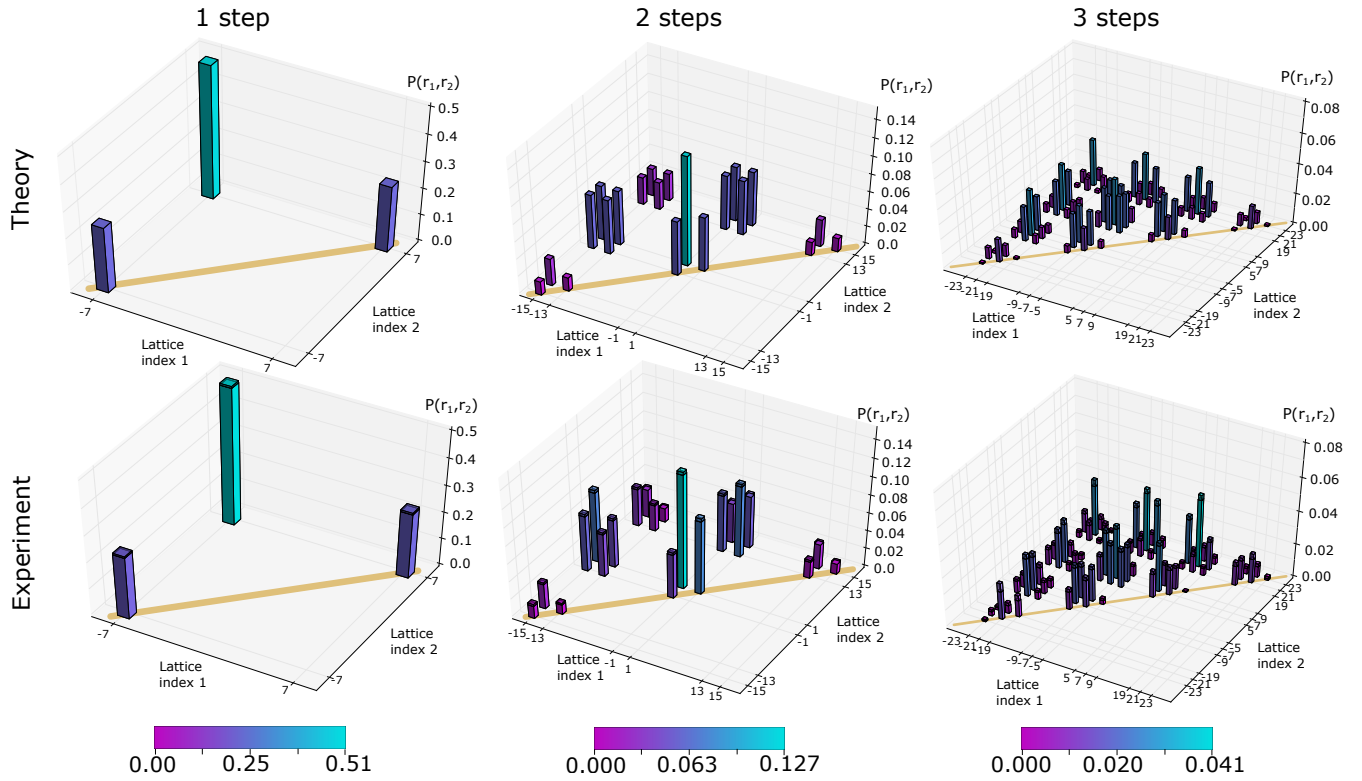
Supplementary Figure 5. **Theoretical distribution and experimental reconstruction of the 2D-QW with distinguishable particles.** The theoretical distribution was computed by setting $c_0 = 0$, corresponding to the visibility of distinguishable particles. The same linearization procedure employed in the main text for indistinguishable particles was performed to obtain a representation of the experimental data. Shaded regions on top of each bar correspond to the experimental error at one standard deviation. The error bars were obtained thorough a bootstrapping approach. The bunching probabilities are highlighted by the yellow line.

C. Violation Inequality

In order to estimate the *non-classicality* of our experimental distribution, we employed the inequality introduced in Supplementary Ref. [10, 11]. More specifically, classical light has to satisfy the following condition:

$$\mathcal{V}(\mathbf{m}_1, \mathbf{m}_2) = \frac{2}{3}\sqrt{\Gamma^{(cl)}_{\mathbf{m}_1,\mathbf{m}_1}\Gamma^{(cl)}_{\mathbf{m}_2,\mathbf{m}_2}} - \Gamma^{(cl)}_{\mathbf{m}_1,\mathbf{m}_2} < 0. \tag{24}$$

where $\Gamma^{(cl)}_{\mathbf{m}_1,\mathbf{m}_2}$ is the classical probability that the light exits from the $\mathbf{m}_1$ and $\mathbf{m}_2$ output ports of an interferometer. The action of the interferometer is described by a unitary matrix $\mathcal{U}$. The evolution of 2D-QW with g-plates is equivalent to the action of an interferometer with unitary matrix given by $\mathcal{U} = U^t$ at each step t. The output modes of 2D-QW interferometer are equivalently given by $\mathbf{m} = \mathbf{r}, \sigma$ where $\mathbf{r}$ is the position on the lattice and $\sigma = \uparrow, \downarrow$. By measuring the final distribution of 2D-QW we trace away the polarization state. For this reason we do not have a direct access to $\Gamma_{\mathbf{r}_1,\sigma_1,\mathbf{r}_2,\sigma_2}$. Hence, we recast Supplementary Equation (24) in terms of the measured values of $\Gamma_{\mathbf{r}_1,\mathbf{r}_2} = \sum_{\sigma_1,\sigma_2}\Gamma_{\mathbf{r}_1,\sigma_1,\mathbf{r}_2,\sigma_2}$. In order to do that, we sum the violation inequalities for the fixed positions $\mathbf{r}_1$ and $\mathbf{r}_2$ on the lattice:

$$\sum_{\sigma_1,\sigma_2}\mathcal{V}(\mathbf{r}_1,\sigma_1,\mathbf{r}_2,\sigma_2) = \frac{2}{3}\sum_{\sigma_1,\sigma_2}\sqrt{\Gamma^{(cl)}_{\mathbf{r}_1,\sigma_1,\mathbf{r}_1,\sigma_1}\Gamma^{(cl)}_{\mathbf{r}_2,\sigma_2,\mathbf{r}_2,\sigma_2}} - \Gamma^{(cl)}_{\mathbf{r}_1,\mathbf{r}_2} < 0. \tag{25}$$

By exploiting the inequality:

$$\sqrt{\sum_i a_i} < \sum_i \sqrt{a_i}, \tag{26}$$

we can write the Supplementary Equation (25) as:

$$\frac{2}{3}\sqrt{\sum_{\sigma_1}\Gamma^{(\mathrm{cl})}_{\mathbf{r}_1,\sigma_1,\mathbf{r}_1,\sigma_1}\sum_{\sigma_2}\Gamma^{(\mathrm{cl})}_{\mathbf{r}_2,\sigma_2,\mathbf{r}_2,\sigma_2}}-\Gamma^{(\mathrm{cl})}_{\mathbf{r}_1,\mathbf{r}_2}<0. \tag{27}$$

By using the definition of $\Gamma_{\mathbf{r}_1,\mathbf{r}_1}$ and $\Gamma_{\mathbf{r}_2,\mathbf{r}_2}$ it can be further rewritten as:

$$\frac{2}{3}\sqrt{(\Gamma^{(\mathrm{cl})}_{\mathbf{r}_1,\mathbf{r}_1}-\Gamma^{(\mathrm{cl})}_{\mathbf{r}_1,\uparrow,\mathbf{r}_1,\downarrow}-\Gamma^{(\mathrm{cl})}_{\mathbf{r}_1,\downarrow,\mathbf{r}_1,\uparrow})(\Gamma^{(\mathrm{cl})}_{\mathbf{r}_2,\mathbf{r}_2}-\Gamma^{(\mathrm{cl})}_{\mathbf{r}_2,\uparrow,\mathbf{r}_2,\downarrow}-\Gamma^{(\mathrm{cl})}_{\mathbf{r}_2,\downarrow,\mathbf{r}_2,\uparrow})}-\Gamma^{(\mathrm{cl})}_{\mathbf{r}_1,\mathbf{r}_2}<0. \tag{28}$$

Finally, considering that $\Gamma_{\mathbf{r},\uparrow,\mathbf{r},\downarrow}=\Gamma_{\mathbf{r}\downarrow,\mathbf{r},\uparrow}$ we can write:

$$\mathcal{V}(\mathbf{r}_1,\mathbf{r}_2)=\frac{2}{3}\sqrt{\Gamma^{(\mathrm{cl})}_{\mathbf{r}_1,\mathbf{r}_1}\Gamma^{(\mathrm{cl})}_{\mathbf{r}_2,\mathbf{r}_2}-2\Gamma^{(\mathrm{cl})}_{\mathbf{r}_2,\mathbf{r}_2}\Gamma^{(\mathrm{cl})}_{\mathbf{r}_1,\uparrow,\mathbf{r}_1,\downarrow}-2\Gamma^{(\mathrm{cl})}_{\mathbf{r}_1,\mathbf{r}_1}\Gamma^{(\mathrm{cl})}_{\mathbf{r}_2,\uparrow,\mathbf{r}_2,\downarrow}}-\Gamma^{(\mathrm{cl})}_{\mathbf{r}_1,\mathbf{r}_2}<0. \tag{29}$$

In the case in which $\Gamma_{\mathbf{r}_1,\uparrow,\mathbf{r}_1,\downarrow}$ and $\Gamma_{\mathbf{r}_2,\uparrow,\mathbf{r}_2,\downarrow}$ are theoretically zero, we can use this violation to demonstrate the quantumness of the output distribution.

We applied this non-classicality test to the measured output distributions for indistinguishable particle inputs, shown in the main text. More specifically, we calculated the value $\mathcal{V}(\mathbf{r}_1,\mathbf{r}_2)$, using Supplementary Equation (29), and the corresponding error $\sigma_V(\mathbf{r}_1,\mathbf{r}_2)$, by propagating the experimental error in the distribution. In Figure 6 of the main text we report the complete plots of $\mathcal{V}(\mathbf{r}_1,\mathbf{r}_2)/\sigma_V(\mathbf{r}_1,\mathbf{r}_2)$ for the second and the third step, respectively. It is worth to notice that we compute the violation only for the case in which the relation $\Gamma_{\mathbf{r}_1,L,\mathbf{r}_1,R}=\Gamma_{\mathbf{r}_2,L,\mathbf{r}_2,R}=0$ is satisfied. The presence of output configurations that violate inequality (29) at each step testifies the non-classicality of the obtained distributions. In Table I of the main text, the value of $\mathcal{V}(\mathbf{r}_1,\mathbf{r}_2)/\sigma_V(\mathbf{r}_1,\mathbf{r}_2)$ corresponding to the configuration that provides maximum violation is reported.

Supplementary References

[1] Aharonov, Y., Davidovich, L. & Zagury, N. Quantum random walks. *Phys. Rev. A* **48**, 1687–1690 (1993).

[2] D'Errico, A. *et al.* Two-dimensional topological quantum walks in the momentum space of structured light. *Optica* **7**, 108 (2020).

[3] Slussarenko, S. *et al.* Tunable liquid crystal q-plates with arbitrary topological charge. *Opt. Express* **19**, 4085–4090 (2011).

[4] Hong, C.-K., Ou, Z.-Y. & Mandel, L. Measurement of subpicosecond time intervals between two photons by interference. *Phys. Rev. Lett.* **59**, 2044 (1987).

[5] D'Ambrosio, V., Carvacho, G., Agresti, I., Marrucci, L. & Sciarrino, F. Tunable two-photon quantum interference of structured light. *Phys. Rev. Lett.* **122**, 013601 (2019).

[6] Giordani, T. *et al.* Experimental engineering of arbitrary qudit states with discrete-time quantum walks. *Phys. Rev. Lett.* **122**, 020503 (2019).

[7] Crespi, A. *et al.* Anderson localization of entangled photons in an integrated quantum walk. *Nat. Photonics* **7**, 322 (2013).

[8] Pitsios, I. *et al.* Photonic simulation of entanglement growth and engineering after a spin chain quench. *Nat. Commun.* **8**, 1569 (2017).

[9] Janossy, L. Rate of n-fold accidental coincidences. *Nature* **153**, 165–165 (1944).

[10] Bromberg, Y., Lahini, Y., Morandotti, R. & Silberberg, Y. Quantum and classical correlations in waveguide lattices. *Phys. Rev. Lett.* **102**, 253904 (2009).

[11] Peruzzo, A. *et al.* Quantum walks of correlated photons. *Science* **329**, 1500–1503 (2010).